International Conference on Smart Infrastructure and Construction 2019 (ICSIC):
Driving data-informed decision-making

ice Publishing

DeJong, Schooling and Viggiani
ISBN 978-0-7277-6466-9
https://doi.org/10.1680/icsic.64669.549

CSIC Cambridge Centre for Smart Infrastructure & Construction

ON THE DERIVATION OF RAIL ROUGHNESS SPECTRA FROM AXLE-BOX VIBRATION: DEVELOPMENT OF A NEW TECHNIQUE

T.D. Carrigan, P.R.A. Fidler and J.P. Talbot*

Cambridge University Engineering Department, Cambridge, United Kingdom
** Corresponding author*

ABSTRACT Railhead roughness on railways is a cause of noise and vibration. Corrugation (a periodic form of roughness) can grow rapidly and unpredictably, generating high levels of noise and vibration. An emerging technique for monitoring rail roughness is by use of axle-box accelerometers on in-service trains, which can be more cost-effective than conventional inspection methods. Axle-box accelerometers measure the vibration induced by roughness, rather than the roughness itself, and hence require signal processing techniques to translate this vibration into suitable metrics of the railhead condition, such as a wavelength spectrum of roughness. This paper presents progress towards a new stochastic frequency-domain inverse method that derives wavelength-spectra of rail roughness from axle-box acceleration measurements. This method compensates for the effects of vehicle speed and track dynamic behaviour on axle-box acceleration, which have adversely affected previous methods that, for example, rely on calibration on a reference section of track or simply take the RMS of the axle-box acceleration. The practical implications of processing and presenting measurements in the frequency domain are discussed, including the effect of varying vehicle speed and the trade-off between resolution and statistical accuracy. An initial algorithm is proposed and demonstrated through time-domain simulations of a theoretical vehicle-track model. Accurate derivation of roughness from axle-box acceleration will facilitate future development of autonomous monitoring systems fitted to in-service trains that continuously 'map' the condition of a rail network in real time, enabling more efficient and proactive scheduling of rail maintenance.

Notation

f: frequency

ω: angular frequency ($2\pi f$)

λ: wavelength

γ: wavenumber ($2\pi/\lambda$)

v: vehicle speed

$S_{aa}(\omega)$: PSD (power spectral density) function of axle-box acceleration at frequency ω

$S_{\delta\delta}(\omega)$: PSD function of rail roughness at frequency ω as seen by a vehicle moving at speed v

$S_{\delta\delta}(\gamma)$: PSD function of rail roughness at wavenumber γ

1. Introduction

Degradation of railway track often leads to increases in environmental noise and vibration, as well as accelerated wear on vehicle and track components. This is a concern for railway operators as it can cause disturbance in track-side buildings and hinder the expansion of railway networks in densely populated areas. One form of degradation involves an increased roughness of the railhead. In extreme cases, this forms a quasi-periodic pattern, known as corrugation, which can initiate at an unpredictable time and grow rapidly, particularly in high-traffic urban railway systems (Grassie, 2012). Rail corrugation is found at wavelengths ranging from 30 mm to 1 m and can cause ground-borne noise as well as airborne noise (Grassie, 1996). Ground-borne noise is vibration at frequencies from 20 to 250 Hz that re-radiates as noise inside buildings.

Typically, rail roughness is measured using manual trolleys or dedicated inspection trains. These methods tend to be costly and time consuming. A more efficient method to monitor roughness is to use sensors on in-service trains — specifically, accelerometers on their axle-boxes. Axle-box accelerometers have been used in many research studies to identify high levels of rail roughness and corrugation (Bocciolone *et al.*, 2007; Bongini *et al.*, 2012; Salvador *et al.*, 2016) as well as isolated defects such as squats (Molodova *et al.*, 2011). Accelerometers are more suitable for in-service vehicles compared to laser- or physical-contact-based roughness measurement devices used on inspection trains, due to the latter devices' high maintenance requirements (Weston *et al.*, 2015). Data from these accelerometers, along with positioning data, have the potential to 'map' a railway network in real time in terms of its propensity to generate vibration. This is demonstrated in Section 2 by measurements of axle-box acceleration that were taken on the West Midlands Metro (WMM) tram network in the UK.

The measurements in Section 2 are presented as simple root-mean-square (RMS) plots. Existing analysis methods like this typically give only a qualitative indication of railhead condition and are affected by variations in vehicle speed and track dynamic behaviour. This is because the accelerometers measure the vibration induced by roughness, rather than the

roughness itself, so roughness needs to be derived using signal processing techniques. Moreover, it is preferred to present roughness measurements as a wavelength spectrum rather than RMS, for example, because rail corrugation appears as a narrow peak in the wavelength spectrum.

Bongini *et al.* (2012) used an axle-box-accelerometer-based instrument (known as HSRCA — high-speed rail corrugation analyser) to measure rail roughness on several sections of track in France. This was calibrated on a reference section of track that was directly measured using a corrugation analysis trolley (CAT). Both the CAT and HSRCA instruments present measurements as third-octave-band wavelength spectra according to EN 15610 (CEN, 2009). The HSRCA gave roughness measurements accurate to 1 μm where the vehicle speed and track properties matched the calibration reference, but deviations in speed and track properties significantly affected the HSRCA's measurements, as well as many other analyses of axle-box acceleration. Therefore, there is a clear need for a better algorithm to derive the railhead roughness spectrum from axle-box acceleration that remains accurate with variations in vehicle speed and track dynamic behaviour.

Section 3 presents an initial algorithm for estimating the roughness spectrum in the frequency domain. As this works with spectra of finite-length signals, practical considerations for use of spectra are discussed, including the trade-off between statistical accuracy, spatial resolution along the track and wavelength resolution in Section 3.1. Variations in vehicle speed within a sample of axle-box acceleration can cause smearing in the frequency components when translating from the time domain to the spatial domain, and this is evaluated in Section 3.5.

A time-domain simulator is developed to evaluate this algorithm, and its operation is described in Section 4. The simulator is based on a simple model of a lumped wheel mass moving along a track, represented as an Euler beam on a single-layer viscoelastic foundation. Section 4.3 presents simulation results of a 22-m section of track with rail roughness and corrugation, traversed at different speeds.

The ultimate objective is to present railhead roughness spectra in third-octave bands, as defined in standards such as EN 15610 (CEN, 2009) and as preferred by railway operators. In this paper, Welch's method is used to calculate power spectral density functions based on the recommendations in EN 15610, which are presented at full resolution to demonstrate the roughness derivation algorithm.

2. Field measurements

A field measurement study was performed to demonstrate the use of axle-box accelerometers on in-service trains and trams to monitor the railhead roughness over an entire network. Vertical accelerometers were fitted to the axle-beams on one of the CAF Urbos 3 trams used on the West Midlands Metro (WMM) link between Wolverhampton and Birmingham. The accelerometer signals were recorded continuously, along with the tram's location and speed as measured by a GPS receiver, and were uploaded to a data server via a wireless LAN link in the depot. Details of the tram and recording system can be found in Fidler *et al.* (2017).

RMS values of the measured acceleration were taken over consecutive 50-metre sections of track. The RMS values over the first 9.5 km of the WMM track from Wolverhampton are plotted in Figure 1 for a selection of full days from April 2017 to October 2018. The tram passes over the sections of track at least 10 times each day, and data from multiple passes are averaged together in the RMS values to improve accuracy.

On April 2017, the on-street tram track between The Royal and Priestfield had very high roughness levels, which correlated with high acceleration measurements. This section of track underwent replacement work from June to December 2017. The acceleration measurements are much lower on the replaced track section (January 2018 onwards) and are in line with the other low-roughness sections of the network.

The RMS levels are very consistent over time in many of the track sections. Seasonal variation is evident in some sections — changes in track stiffness with weather conditions as well as vehicle speed at each section of track affect axle-box

Figure 1 RMS acceleration measured along the West Midlands Metro network

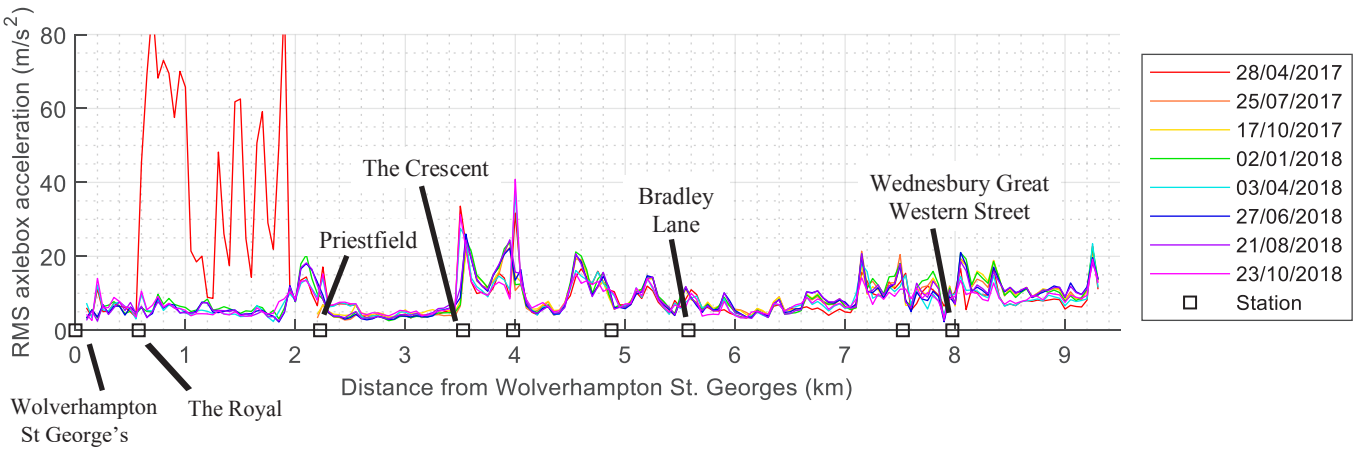

acceleration, and these effects will be mitigated by the roughness derivation algorithm in this research.

The analysis of RMS acceleration proves that accelerometers can detect changes in rail roughness. However, measurements of the actual rail roughness are preferred by rail operators, and RMS acceleration is not an accurate measure of rail roughness. Instead, a new technique is developed to derive spectra of rail roughness from axle-box acceleration.

3. Deriving roughness spectra from axle-box acceleration

Assuming rail roughness and axle-box acceleration as stationary random signals, the power spectral density (PSD) of axle-box acceleration $S_{aa}(\omega)$ is related to the PSD of the roughness $S_{\delta\delta}(\omega)$ as seen by a wheel moving along the rail at speed v, according to random process theory (Newland, 1993: p. 72), by

$$S_{aa}(\omega) = |H(\omega)|^2 S_{\delta\delta}(\omega) \tag{1}$$

where ω is the angular frequency in rad/s and $H(\omega)$ is the frequency response function governing the linear process between the roughness excitation and the axle-box acceleration response. $H(\omega)$ can be derived by considering that the vertical wheel-rail contact forces F are equal and opposite, and that the roughness profile δ and wheel-rail contact spring are interposed between the wheel y_w and rail y_r vertical displacements, i.e.

$$y_w = y_r + \delta - \frac{F}{k_H} \tag{2}$$

where k_H is the contact spring stiffness. Substituting the point receptance functions of the wheel $H_w(\omega) = y_w/F$ and rail $H_r(\omega) = -y_r/F$ into Equation (2) and eliminating F gives

$$H(\omega) = \frac{-\omega^2 y_w(\omega)}{\delta(\omega)} = -\omega^2 \left(\frac{H_w(\omega)}{H_w(\omega) + H_r(\omega) + k_H^{-1}} \right) \tag{3}$$

where $-\omega^2 y_w(\omega)$ is the wheel vertical acceleration in the frequency domain, assuming that the axle-box moves with the wheel. Translating $S_{\delta\delta}(\omega)$ from the frequency ($\omega = 2\pi f$) domain to the wavenumber ($\gamma = 2\pi/\lambda$) domain according to vehicle speed v, Equation (1) yields the rail roughness PSD as

$$S_{\delta\delta}\left(\gamma = \frac{\omega}{v}\right) = v S_{\delta\delta}(\omega) = \frac{v}{|H(\omega)|^2} S_{aa}(\omega) \tag{4}$$

Equation (4) forms the basis of the present roughness derivation algorithm. The calculation of the PSD $S_{aa}(\omega)$ is discussed in the following sections.

3.1 PSD periodogram calculation

The PSD of a random signal can be estimated using the square-magnitude Fourier transform of a finite sample of the signal, which is called a periodogram. The single-sided periodogram of a sample of acceleration $a_s(t)$, represented by the discrete series $a_s[n]$, is computed by

$$S_{aa}(\omega) = \frac{2|\mathcal{F}(w[n] a_s[n])|^2}{D_2 f_s} \tag{5}$$

where $w[n]$ is a Hann window of the same length as $a_s[n]$, f_s is the sampling frequency,

$$\mathcal{F}(y[n]) = \sum_{n=0}^{N-1} y[n]\, e^{-\frac{2i\pi nk}{N}}, \quad k = 0, 1, \ldots, \frac{N}{2} \tag{6}$$

is the single-sided discrete Fourier transform, and

$$D_2 = \sum_{n=0}^{N-1} w^2[n] \tag{7}$$

is the sum-square of the window function, which compensates for the window's attenuation on the periodogram (Heinzel *et al.*, 2002).

The frequency spectrum of axle-box acceleration can contain relatively sharp peaks, caused by corrugation as well as resonances in the vehicle-track dynamic response. Peaks in the spectra can cause spectral leakage, which increases and corrupts the spectral estimates at frequencies surrounding the peak (or the entire spectrum in severe cases). This is why a Hann window is applied to the sample to reduce spectral leakage.

3.2 Statistical accuracy

The Fourier periodogram of a sample is an estimate of the random signal's true PSD. Its statistical accuracy is the ratio of standard deviation to ensemble mean σ/m of each data point in the periodogram. This depends on the effective noise bandwidth B_e and the length T of the signal over which the periodogram is calculated, and is given by (Newland, 1993: p. 137)

$$\frac{\sigma}{m} \approx \frac{1}{\sqrt{B_e T}} \tag{8}$$

For a single periodogram, $B_e = 1/T$, so the standard deviation is equal to the mean, $\sigma = m$, which is not acceptable. Therefore, the statistical accuracy is improved by using Welch's method, which averages together multiple periodograms. In this method, the section of track is split into a number K of consecutive segments of equal length. The periodograms of the portions of signal associated with each of these segments are taken using Equation (5) and averaged together to calculate the final PSD for the section of track. This improves the statistical accuracy to

$$\frac{\sigma}{m} \approx \frac{1}{\sqrt{K}} \tag{9}$$

but widens the frequency resolution and bandwidth by a factor of K.

As the Hann window tapers the signal off at both ends, the segments in Welch's method are overlapped with each other by 50% so that the samples in the signal are more equally represented in the PSD. Both the Hann window and 50% overlap are specified in EN 15610 (CEN, 2009) for calculating rail roughness spectra — the statistical accuracy in Equation

(9) still approximately holds with the use of this combination (Harris, 1978).

3.3 Sampling frequency

The sampling frequency determines the highest frequency of axle-box acceleration that can be measured. This should be set according to the shortest wavelength λ to be measured (typically 20–30 mm for rail roughness) and the vehicle's top speed v_{max}. The WMM tram's top speed is about 20 m/s. The highest measured frequency is

$$f_{max} = \frac{v_{max}}{\lambda_{min}} \tag{10}$$

According to the Nyquist criterion, the sampling frequency should be at least double the highest frequency, so in order to measure roughness at wavelengths down to 30 mm at a speed of 20 m/s, for example, the sampling frequency must be at least 1.34 kHz.

3.4 Trade-off in accuracy and resolution

There is a trade-off between statistical accuracy, wavenumber resolution and spatial resolution along the track. The wavenumber resolution $\Delta\gamma$ is related to the track segment length l_s by

$$\Delta\gamma = \frac{2\pi}{l_s} \tag{11}$$

and determines the longest wavelength that can be measured i.e. $\lambda_{max} = l_s$. If the spectrum is represented in third-octave bands, EN 15610 (CEN, 2009) recommends that the segment length is at least four times the longest wavelength band, so if the longest wavelength to be measured is 1 m, the segment length required to give a frequency resolution suitable for the longest-wavelength third-octave bands is 4 m. The choice of 1 m wavelength corresponds to the lower frequency bound of ground-borne noise (20 Hz) at the WMM tram's top speed of about 20 m/s (70 km/h), and corrugation is typically not longer than 1 m in wavelength (Grassie, 2009).

On choosing a suitable segment length, the number of segments K per track section sets the trade-off between spatial resolution along the track and statistical accuracy. For a third-octave spectrum, this trade-off applies mostly to the longest wavelength band of the spectrum – the accuracy increases for shorter wavelength third-octave bands as an increasing number of the narrowband spectrum's frequency bins are averaged together. The choice of spatial resolution depends on the requirements for railway maintenance operations, considering the aim of monitoring noise and vibration emissions due to roughness as well as reasonable run lengths of rail grinding operations, etc. This choice could vary at different wavelength ranges, considering factors of noise propagation at different frequencies as well as the propensity to damage the vehicle and track. EN 15610 (CEN, 2009) recommends a section length of 60 times the longest wavelength third-octave band being measured to attain sufficient statistical accuracy. If the longest wavelength is 1 m, this would require $K = 29$ to give a section length of 60 m. For testing the roughness derivation algorithm in the simulator, $K = 10$ is used in this work, giving a section length of 22 m (considering the 50% i.e. 2 m overlap between segments) and hence a spatial resolution of 20 m if the sections are overlapped by 2 m. The wavelength third-octave bands below 0.33 m still comply with EN 15610 for 22-m sections.

3.5 Effect of varying vehicle speed on PSD — wavelength smearing

The roughness PSD is derived from the axle-box acceleration PSD in the frequency domain before it is translated into the wavelength domain according to Equation (4). An issue occurs when the vehicle speed is varying within the section of track that the PSD is taken over, because the translation into the wavelength domain assumes a constant speed over that section. This causes the wavelength spectrum to be 'smeared' since each wavelength bin may represent a range of wavelengths.

Wavelength smearing can be minimised by taking the PSD over shorter sections — Welch's method is advantageous in that respect because it averages together the spectra of a series of short segments rather than processing the spectrum of a longer section of track. Here, Welch's method is adapted so that the roughness derivation processing and translation to the wavelength domain is applied to individual segments according to the average velocities within these segments, rather than the entire track section.

Consider the vehicle moving onto a new track segment at speed v_1 and undergoing constant acceleration a until it leaves the segment at speed v_2. The amount of wavelength smearing that occurs in this segment can be quantified as the ratio between the actual wavelength λ_{actual} of data acquired at speed v and the wavelength bin λ_{avg} in which the data is placed assuming an average speed v_{avg} along the segment. This is given by

$$\frac{\lambda_{actual}}{\lambda_{avg}} = \frac{v}{v_{avg}} \tag{12}$$

The ratio is expressed here as a positive percentage difference from unity by

$$e_\lambda = 100\% \times \begin{cases} \frac{\lambda_{actual}}{\lambda_{avg}} - 1, & \lambda_{actual} \geq \lambda_{avg} \\ \frac{\lambda_{avg}}{\lambda_{actual}} - 1, & \lambda_{actual} < \lambda_{avg} \end{cases} \tag{13}$$

The average velocity v_{avg} within the track segment, of length l_s, is given by

$$v_{avg} = \frac{v_1+v_2}{2} = \frac{l_s}{T_s} \tag{14}$$

where T_s is the travel time along the segment:

$$T_s = \frac{-v_1+\sqrt{v_1^2+2al_s}}{a} \tag{15}$$

The percentage difference increases with increasing segment length and acceleration, and with decreasing starting speed v_1. The greatest smearing, as a percentage difference, occurs at the

ends of the segment where the speed differs greatest from the average speed within the segment. Values of percentage difference at the ends of a 4-m-long segment are given in Table 1 for an acceleration of 1.6 m s^{-2} (the maximum acceleration observed on the WMM tram) and a range of starting speeds. Smearing can be kept below 19% by discarding segments in which vehicle speed falls below 3.8 m/s, for example. It is worth noting that as a vehicle accelerates in a section of track, most of the smearing will typically occur in the one segment in which the vehicle speed is lowest. The averaging of periodograms from multiple segments will reduce the effect of smearing associated with any single segment.

Table 1 Wavelength smearing within a periodogram representing a track segment of length 4 m due to a constant vehicle acceleration of 1.6 m s^{-2}

Start speed v_1	End speed v_2	Smearing at v_1	Smearing at v_2
0	3.58	∞	∞
1	3.71	136%	58%
3.8	5.22	19%	16%
5.5	6.56	10%	9%

3.6 Summary of roughness derivation algorithm

On account of the above considerations, the full procedure for deriving the rail roughness spectrum from axle-box acceleration data, recorded along with vehicle position and speed, is as follows. The track is split into consecutive sections over which roughness PSDs are to be calculated. Each section is split into K segments of equal length, of at least four times the longest wavelength to be measured. The time-domain acceleration signal is aligned with the segment boundaries according to the vehicle position and speed so that the portions of signal associated with each segment of track can be isolated. The periodograms $S_{aa}(\omega)$ of the signal portions corresponding to the segments are taken using Equation (5). These are then translated to the wavelength-domain roughness periodograms $S_{\delta\delta}(\lambda)$ using Equation (4) and substituting $\lambda = 2\pi/\gamma$. The resulting roughness periodograms associated with each section of track are then averaged together to calculate the final roughness PSDs for each track section.

4. Simulator

A vehicle-track simulator is developed in order to test the roughness derivation algorithm. The simulator models an idealised dynamic vehicle-track system to calculate the axle-box acceleration signal in the time domain for a given rail roughness profile. A time-domain simulator is used as it can simulate arbitrary variations in the track's properties as well as non-linear behaviour, enabling future studies on their effects on the derived roughness.

The acceleration signal from the simulator is then fed into the roughness derivation algorithm under test, which derives a roughness spectrum from the acceleration signal that is then compared to the spectrum of the actual roughness profile. This process is illustrated in Figure 2.

A random roughness profile is generated with a spectral envelope according to the third-octave-band roughness limit spectrum in BS EN ISO 3095:2013 (BSI, 2013), shown in Figure 3. This spectrum is close to typical roughness spectra of well-maintained railway track (Grassie, 2012).

Figure 3 BS EN ISO 3095:2013 third-octave-band rail roughness limit spectrum

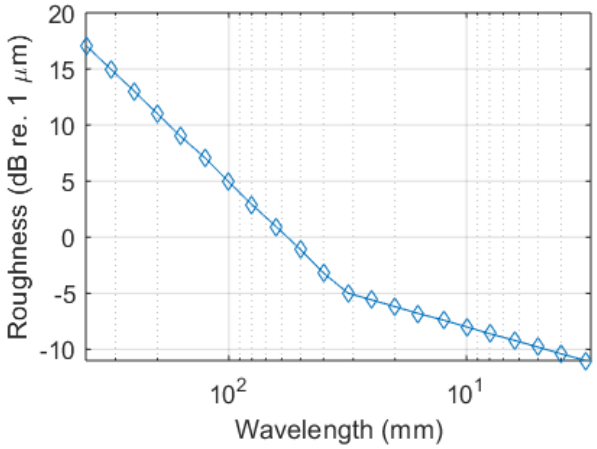

4.1 Vehicle-track model

The simulator is based on a coupled vehicle-track model with a roughness profile interposed between the wheel and rail, as illustrated in Figure 4. The track is based on Koh *et al.*'s (2003) model of an Euler beam on a continuous viscoelastic foundation that is discretised into finite elements. The motion equations of the track elements are formulated in the vehicle's reference frame such that the elements are 'moving' under the vehicle. The vehicle's unsprung mass is modelled as a single lumped mass, which is connected to the middle node of the track model via a Hertzian contact spring.

The equation of motion for the moving-element track model containing N beam elements is

$$\mathbf{M}_s\ddot{\mathbf{z}}(t) + \mathbf{C}_s\dot{\mathbf{z}}(t) + \mathbf{K}_s\mathbf{z}(t) = \mathbf{P}_s(t) \qquad (16)$$

in terms of the mass $\mathbf{M}_s$, damping $\mathbf{C}_s$ and stiffness $\mathbf{K}_s$ matrices, force vector $\mathbf{P}_s(t)$, and displacement and rotation coordinates $\mathbf{z} = [y_1 \quad \theta_1 \quad y_2 \quad \theta_2 \quad \cdots \quad y_{N+1} \quad \theta_{N+1}]$. These system

Figure 2 Process for testing the roughness derivation algorithm

matrices are formed by connecting together N beam elements, whose matrices $\mathbf{M}_e$, $\mathbf{C}_e$, and $\mathbf{K}_e$ are derived by Koh *et al.* (2003) in terms of vehicle speed, rail bending stiffness and mass per unit length, and the stiffness k' and damping c' of the viscoelastic foundation. The two ends of the track are clamped by deleting the first and last nodes.

Figure 4 Moving-element model of a beam on viscoelastic foundation with a lumped wheel mass coupled to the middle element via a roughness profile

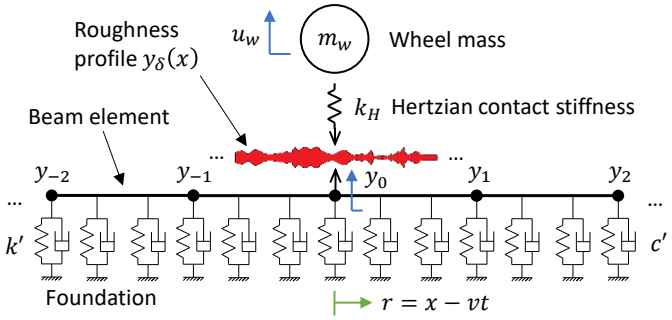

Travelling waves in the rail beam reflect at the clamped ends. This is unwanted as it is intended to simulate an infinitely-long track. To minimise these reflections, the model is made sufficiently long and the foundation damping is increased near both ends to damp out reflections.

The equation of motion for the complete vehicle-track model,

$$\mathbf{M}\ddot{\mathbf{z}}(t) + \mathbf{C}\dot{\mathbf{z}}(t) + \mathbf{K}\mathbf{z}(t) = \mathbf{P}(t) \tag{17}$$

is derived by coupling the wheel mass m_w via contact stiffness k_H to the middle node of the track model according to

$$\mathbf{M} = \begin{bmatrix} \mathbf{M}_s & 0 \\ 0 & m_w \end{bmatrix} \tag{18}$$

$$\mathbf{C} = \begin{bmatrix} \mathbf{C}_s & 0 \\ 0 & 0 \end{bmatrix} \tag{19}$$

$$\mathbf{K} = \begin{bmatrix} \mathbf{K}_s + [k_H]_{(N/2)+1,(N/2)+1} & -k_H \\ -k_H & k_H \end{bmatrix} \tag{20}$$

The roughness profile $y_\delta(x)$ is inserted between the wheel and rail, which applies a wheel-rail force according to

$$\mathbf{P}(t) = \begin{bmatrix} [-k_H]_{(N/2)+1} \\ k_H \end{bmatrix} y_\delta(t) \tag{21}$$

where $y_\delta(t)$ represents the roughness as it appears at the wheel-rail contact at time t as the vehicle moves along the profile. The notation $[k_H]_{(N/2)+1,(N/2)+1}$ signifies a square matrix of size equal to that of $\mathbf{K}_s$, with the diagonal element corresponding to the displacement coordinate of the $(N/2+1)^{\text{th}}$ node equal to k_H and all other elements zero. $[-k_H]_{(N/2)+1}$ is a column vector of length equal to the height of $\mathbf{K}_s$, with the element corresponding to the displacement coordinate of the $(N/2+1)^{\text{th}}$ node equal to $-k_H$ and all other elements zero. (The number of beam model elements N is always even-numbered.)

The equation of motion (17) is solved using MATLAB's ODE solver 'ode23t' along a given roughness profile and with a set of vehicle and track parameters that determine the matrices. 'ode23t' is used as it is the most efficient solver for this simulation, which is run at a relative tolerance of ±0.05. The wheel's vertical acceleration is then extracted from the simulation results and taken as the axle-box acceleration signal. This signal is then fed into the roughness derivation algorithm, summarised in Section 3.6, to calculate PSDs of derived roughness over one or more consecutive sections of track. The derived roughness PSDs are then compared with the PSDs of actual roughness taken over the same sections of track.

4.2 Method

The simulator is configured with the model parameters listed in Table 2, which represent a typical mainline vehicle (Sheng *et al.*, 2004) and ballasted track (Thompson, 2009: p. 42). The foundation damping c' of 77.46 kN s m^{-2} is chosen to give a damping ratio of 0.5, which corresponds to a loss factor of 1 at resonance (Sheng *et al.*, 2004). The damping ratio ζ is related to the foundation damping, stiffness and rail mass per unit length by

$$\zeta = \frac{c'}{2\sqrt{m_r' k'}} \tag{22}$$

Table 2 Parameters for the track and vehicle model

Parameter	Symbol	Value
Rail bending stiffness	EI	6.42 MN m^2
Rail mass per unit length	m_r'	59.9 kg m^{-1}
Foundation stiffness per unit length	k'	100 MN m^{-2}
Foundation viscous damping per unit length	c'	77.46 kN s m^{-2}
Hertzian contact stiffness	k_H	2.7 GN m^{-1}
Vehicle unsprung mass per wheel	m_w	1750 kg

The track comprises 30.5 m of random roughness generated at wavelengths from 20 mm to 1 m according to the ISO 3095:2013 spectrum in Figure 3 extrapolated up to 1 m wavelength. Corrugation is simulated by superimposing a sine wave of wavelength 0.1 m and peak amplitude 50 µm onto the random roughness profile. The first and last 0.5 m of roughness are tapered by half-cosines to reduce the initial transient. The same roughness profile is used in all simulations.

The PSDs of the actual roughness profile and simulated axle-box acceleration are taken over 22 m of the track's length, starting at 5 m to avoid the initial transient and capture the model's steady-state response. The actual roughness PSD is calculated using Welch's method, by splitting the 22 m track section into ten 4 m segments overlapped by 50%, and

averaging periodograms of the portions of roughness profile within each segment, as described in Section 3.2.

The roughness derivation procedure in Section 3.6 is used to derive the PSD of roughness from axle-box acceleration using the same track segments. The vehicle and track receptances in Equation (3) are calculated as follows with the same parameters in Table 2: the vertical point receptance $H_r(\omega)$ of the beam on elastic foundation, representing the track in Figure 4, is given by (Thompson, 2009: p. 44)

$$H_r(\omega) = \frac{-1-i}{4EI\gamma^3(\omega)} \tag{23}$$

$$\gamma(\omega) = \sqrt[4]{\frac{m'_r\omega^2 - i\omega c' - k'}{EI}}\Bigg|_{\text{+ve real part, −ve imaginary part}} \tag{24}$$

where the solution of the 4th root with positive real and negative imaginary parts is taken as $\gamma(\omega)$, and the point receptance of the wheel $H_w(\omega)$, modelled as a lumped mass representing the vehicle's unsprung mass m_w, is

$$H_w(\omega) = \frac{-1}{\omega^2 m_w} \tag{25}$$

4.3 Results

4.3.1 Results at constant vehicle speed: The simulation was run at vehicle speeds of 5 m/s, 10 m/s and 20 m/s. Figure 5 shows how speed affects the axle-box acceleration spectrum for the same roughness profile. The 0.1-m-wavelength corrugation peak moves from 50 Hz at 5 m/s to 200 Hz at 20 m/s, so a higher speed clearly results in higher frequency for a given wavelength. This is not a simple translation because the filtering effect of the track's dynamic behaviour is fixed in frequency, so the vehicle-track resonance at 44 Hz appears in all three spectra. Moreover, the vibration levels increase overall with vehicle speed.

The actual and derived roughness PSDs are plotted in Figure 6, Figure 7 and Figure 8 for simulations at vehicle speeds of 5, 10 and 20 m/s respectively. In all 3 cases, the derived roughness spectrum follows the actual spectrum very closely, showing how well the roughness derivation algorithm accounts for vehicle speed and vehicle-track dynamics.

4.3.2 Results with varying vehicle speed: Further simulations were run with the vehicle accelerating at a constant 1.6 m s^{-2} from standstill. The resulting roughness PSDs are taken over 22 m sections of track where the vehicle is accelerating from 5.5 to 10 m/s in Figure 9, from 3.8 to 9.2 m/s in Figure 10 and from 1.0 to 8.4 m/s in Figure 11. The derived-roughness periodograms of each segment are translated from the frequency domain to the wavelength domain using the average vehicle speed within the segment, i.e. $v = v_{avg}$ in Equation (4). The wavelength content of the corrugation peak at 100 mm is evidently smeared outwards in the derived roughness PSD — this smearing is greater the lower the vehicle speed. Smearing is caused by the vehicle speed varying within the segments of track over which the windowed periodograms are taken, as discussed in Section 3.5.

The three roughness spectra at varying vehicle speeds are re-plotted as EN 15610 third-octave-band spectra in Figure 12, where the real-world effect of smearing can be seen more clearly. The first plot of derived roughness, with the vehicle accelerating from 5.5 to 10 m/s, shows no significant deviation from the actual roughness. Small deviations can be seen in the 3.8–9.2 m plot each side of the corrugation peak at 100 mm wavelength. Smearing is significant in the 1.0–8.4 m/s plot. In all cases, the height of the peak at 100 mm wavelength appears to be unaffected, implying that corrugation can still be identified even in the presence of wavelength smearing.

5. Conclusion

A new technique has been demonstrated to derive rail roughness spectra from axle-box acceleration by compensating for vehicle speed and the transfer function between rail roughness excitation and axle-box response. The algorithm computes the Fourier spectra (periodograms) of portions of the axle-box acceleration time-history, corresponding to short consecutive segments of track, and averages the spectra of a number of segments to both improve statistical accuracy and minimise errors caused by variations in vehicle speed. The transfer function compensation and the translation from the frequency domain to the wavenumber domain are applied to the individual segment spectra before they are averaged. This is accurate to ±1 dB at various constant vehicle speeds and remains reasonably accurate with small relative variations in speed. Assuming that the wheel and rail receptance functions are known exactly, the derived roughness spectrum is very close (within 1 dB) to the actual roughness spectrum as long as the vehicle speed is constant or varying by a small percentage within each track segment.

The compromise between statistical accuracy, wavenumber resolution and spatial resolution along the track has been examined. The EN 15610 standard (CEN, 2009) recommends a segment length (which sets the wavenumber resolution) of at

Figure 5 Simulated axle-box acceleration spectra at three vehicle speeds

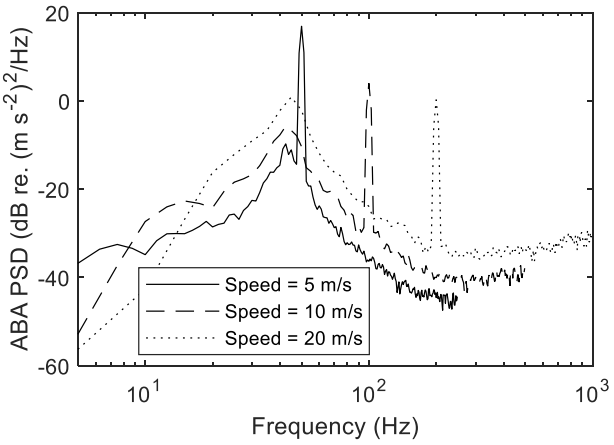

Figure 6 Derived and actual roughness spectra at a vehicle speed of 5 m/s

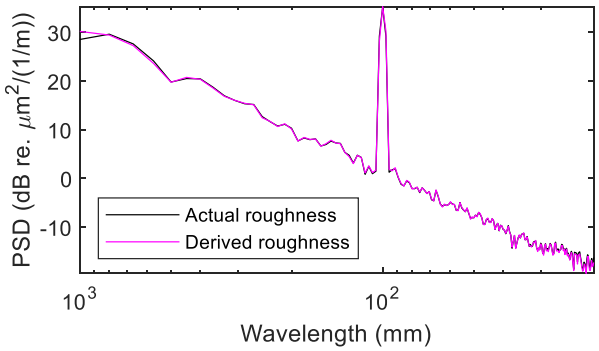

Figure 7 Derived and actual roughness spectra at a vehicle speed of 10 m/s

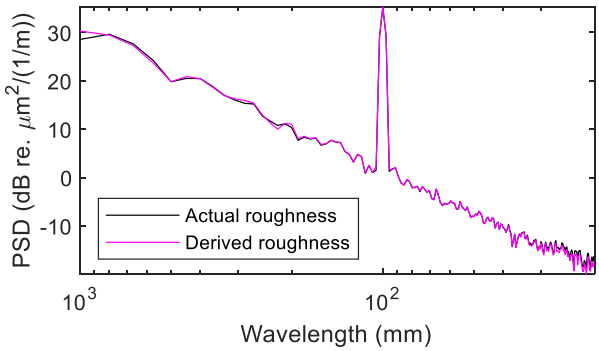

Figure 8 Derived and actual roughness PSDs at a vehicle speed of 20 m/s

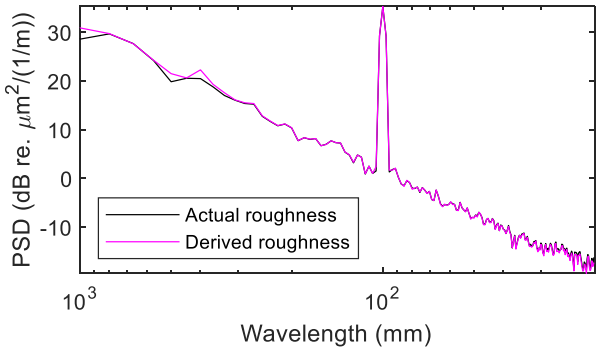

Figure 9 Derived and actual roughness PSDs taken as the vehicle accelerates at 1.6 m s^{-2} from 5.5 m/s to 10 m/s over 22 m of track.

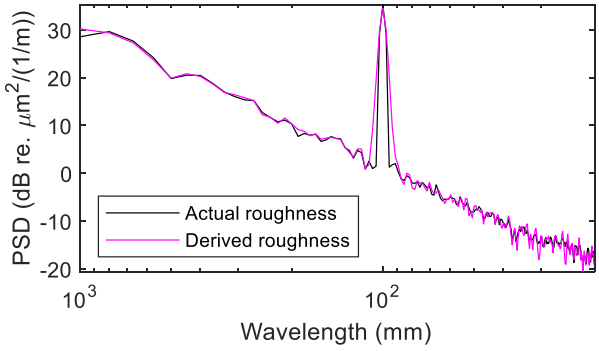

Figure 10 Derived and actual roughness PSDs taken as the vehicle accelerates at 1.6 m s^{-2} from 3.8 m/s to 9.2 m/s over 22 m of track.

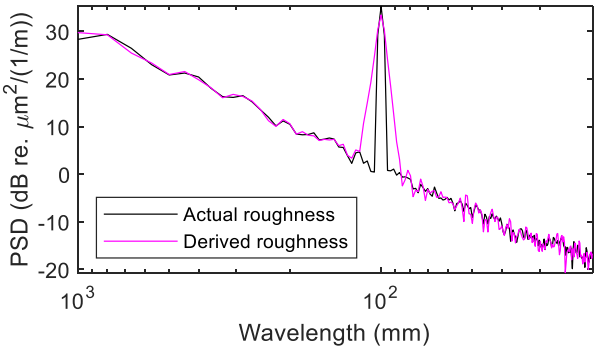

Figure 11 Derived and actual roughness PSDs taken as the vehicle accelerates at 1.6 m s^{-2} from 1.0 m/s to 8.4 m/s over 22 m of track.

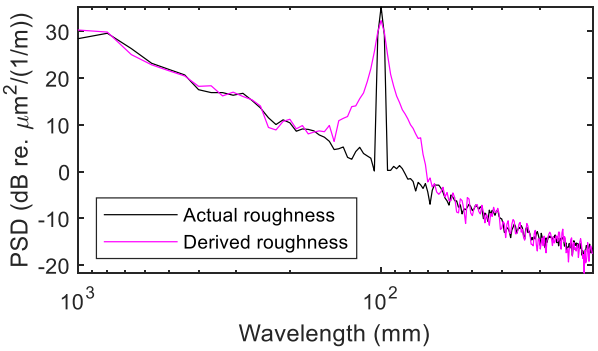

Figure 12 Derived and actual roughness third-octave-band spectra taken as the vehicle accelerates at 1.6 m s^{-2} from various starting speeds over 22 m of track.

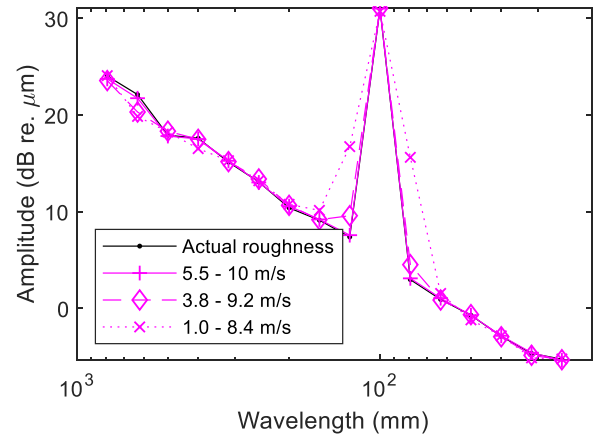

least four times the longest wavelength to be measured. The number of segments over which each roughness spectrum is calculated (by averaging the spectra of these segments) then controls the trade-off between statistical accuracy and spatial resolution (i.e. the length of track section over which each spectrum applies).

The present roughness derivation algorithm requires the dynamic properties of the vehicle and track to be known exactly. While both the wheel and rail receptances can be

measured in principle, neither is straightforward, primarily due to the non-linear stiffness characteristics of components within both the vehicle suspension and the track. In addition, rail receptance can vary significantly at different locations along the track, as well as over time. Further work will therefore investigate the extraction of the dynamic properties of vehicle and track from axle-box acceleration measurements, to enable the accurate derivation of the rail roughness spectrum in practice. Roughness on the wheel also contributes to axle-box acceleration (and vibration emissions in general). Wheel roughness can be similar in amplitude to rail roughness at wavelengths below 0.25 m (Thompson *et al.*, 2018), which leads to errors in the derived rail roughness. Further work will also aim to separate wheel and rail roughness from the axle-box acceleration signal in order to isolate the rail roughness spectrum.

The current simulator assumes a simple, lumped mass on a beam-on-viscoelastic foundation as the underlying vehicle-track model and has been tested on simulated axle-box acceleration data. Refinements will be made progressively to the vehicle-track model and algorithm so that they can represent and compensate for the dynamic response of a range of trackforms. The algorithm, once further developed, will be tested on real measurements of axle-box acceleration and railhead roughness.

6. Acknowledgements

This work is funded by an EPSRC DTP studentship (RG 80792), in collaboration with Project VIMTO (Fidler *et al.*, 2017), a project of the Cambridge Centre for Smart Infrastructure and Construction (EP/I019308/1; EPSRC Impact Acceleration Grant No. EP/K503757/1). Data supporting this paper is available from the University of Cambridge repository at https://doi.org/10.17863/CAM.35687.

7. References

Bocciolone M *et al.* (2007) A measurement system for quick rail inspection and effective track maintenance strategy. *Mechanical Systems and Signal Processing* 21(3): 1242–1254, 10.1016/j.ymssp.2006.02.007.

Bongini E *et al.* (2012) 'Noise mapping' of a railway network: validation and use of a system based on measurement of axlebox vibration. In *Noise and Vibration Mitigation for Rail Transportation Systems* vol. 118 (Maeda T *et al.* (eds)). Springer, Tokyo, Japan, pp. 505–513.

BSI (British Standards Institute) (2013) BS EN ISO 3095:2013: Acoustics - Railway applications - Measurement of noise emitted by railbound vehicles. BSI, London, UK.

CEN (European Committee for Standardisation) (2009) EN 15610:2009: Railway applications - Noise emission - Rail roughness measurement related to rolling noise generation. CEN, Brussels, Belgium.

Fidler PRA *et al.* (2017) Project VIMTO: a new system for the vibration and impact monitoring of tram operations. *SHMII 2017—8th International Conference on Structural Health Monitoring of Intelligent Infrastructure* (Chan T *et al.* (eds)), Brisbane, Australia, pp. 1029–1039, 10.17863/CAM.15237.

Grassie SL (1996) Measurement of railhead longitudinal profiles: a comparison of different techniques. *Wear* 191(1): 245–251, 10.1016/0043-1648(95)06732-9.

Grassie SL (2009) Rail corrugation: characteristics, causes, and treatments. *Proceedings of the Institution of Mechanical Engineers, Part F: Journal of Rail and Rapid Transit* 223(6): 581–596, 10.1243/09544097JRRT264.

Grassie SL (2012) Rail irregularities, corrugation and acoustic roughness: characteristics, significance and effects of reprofiling. *Proceedings of the Institution of Mechanical Engineers, Part F: Journal of Rail and Rapid Transit* 226(5): 542–557, 10.1177/0954409712443492.

Harris FJ (1978) On the use of windows for harmonic analysis with the discrete fourier transform. *Proceedings of the IEEE* 66(1): 51–83, 10.1109/PROC.1978.10837.

Heinzel G *et al.* (2002) *Spectrum and spectral density estimation by the Discrete Fourier transform (DFT), including a comprehensive list of window functions and some new flat-top windows*. Max-Planck-Institut für Gravitationsphysik, Hannover, Germany.

Koh CG *et al.* (2003) Moving element method for train-track dynamics. International Journal for Numerical Methods in Engineering 56(11): 1549–1567, 10.1002/nme.624.

Molodova M *et al.* (2011) Axle box acceleration: Measurement and simulation for detection of short track defects. *Wear* 271(1): 349–356, 10.1016/j.wear.2010.10.003.

Newland DE (1993) *An introduction to random vibrations, spectral and wavelet analysis*, 3rd edn. Longman Scientific & Technical, Essex, UK.

Salvador P *et al.* (2016) Axlebox accelerations: Their acquisition and time–frequency characterisation for railway track monitoring purposes. *Measurement* 82(C): 301–312, 10.1016/j.measurement.2016.01.012.

Sheng X *et al.* (2004) A theoretical model for ground vibration from trains generated by vertical track irregularities. *Journal of Sound and Vibration* 272(3): 937–965, 10.1016/S0022-460X(03)00782-X.

Thompson D (2009) *Railway Noise and Vibration*, 1st edn. Elsevier, London, UK.

Thompson D *et al.* (2018) Assessment of measurement-based methods for separating wheel and track contributions to railway rolling noise. *Applied Acoustics* 140: 48–62, 10.1016/j.apacoust.2018.05.012.

Weston P *et al.* (2015) Perspectives on railway track geometry condition monitoring from in-service railway vehicles. *Vehicle System Dynamics* 53(7): 1063–1091, 10.1080/00423114.2015.1034730.